



Activation of MCM-41 mesoporous silica by transition-metal incorporation for photocatalytic hydrogen production



Shaohua Shen^{a,*}, Jie Chen^a, Ranjit T. Koodali^b, Yongfeng Hu^c, Qunfeng Xiao^c, Jigang Zhou^{c,*}, Xixi Wang^a, Liejin Guo^a

^a International Research Center for Renewable Energy, State Key Laboratory of Multiphase Flow in Power Engineering, Xi'an Jiaotong University, Shaanxi 710049, China

^b Department of Chemistry, University of South Dakota, 414 E. Clark Street, Vermillion, SD 57069, United States

^c Canadian Light Sources Inc., Canadian National Synchrotron Facility, 101 Perimeter Rd, Saskatoon, SK, Canada S7NOX4

ARTICLE INFO

Article history:

Received 4 October 2013

Received in revised form

23 November 2013

Accepted 8 December 2013

Available online 15 December 2013

Keywords:

MCM-41

Mesoporous silica

Transition metal

Photocatalytic

Hydrogen production

ABSTRACT

A series of transition metal incorporated MCM-41 mesoporous silica is successfully synthesized by hydrothermal method, and all of them display optical absorption in ultraviolet-visible light region. Analysis results from different characterization techniques demonstrate that the transition metal ions are well dispersed in the silica framework and mainly in tetrahedral coordination. In comparison to Co and Ni incorporated MCM-41, Fe-MCM-41 shows considerable photocatalytic activity for hydrogen production, without loading any noble metal as cocatalyst. The activation for photocatalytic reaction is induced by the ligand-to-metal charge-transfer (LMCT) excitation of the monometallic centers in the framework-substituted MCM-41. Bimetal co-incorporation is found to be effective for the enhanced photocatalytic activity. For instance, Fe/Ni co-incorporated MCM-41 shows much higher photocatalytic activity for hydrogen production than either Fe or Ni incorporated MCM-41 indicating synergistic effect of co-doping with Fe and Ni. The main reason for the enhanced activity is attributed to the metal-to-metal charge-transfer (MMCT) excitation creating oxo-bridged bimetallic redox sites, which results in efficient charge separation and creation of long-lived electrons and holes to initiate redox reaction.

© 2013 Elsevier B.V. All rights reserved.

1. Introduction

Photocatalytic hydrogen production has attracted extensive attention since the discovery of Fujishima–Honda effect [1], which has shown great potential to realize the conversion of solar energy to split water into hydrogen and oxygen. In the past decades, different kinds of semiconductor materials, including oxides, (oxy)sulfides, (oxy)nitrides, have been developed as photocatalysts for efficient hydrogen production from water [2–7]. Continuous efforts by many groups have resulted in significant advances in the photocatalytic efficiency for hydrogen production by developing novel visible light active semiconducting materials, such as GaN:ZnO solid solutions [8], black TiO₂ [9], and CdZnS nanotwin structures [10], etc. However, exploitation of photocatalysts with high efficiency, high stability, and low cost under visible or solar light irradiation still remains a great challenge, and there is still a long way to go to meet the requirement for practical application of solar hydrogen conversion [5,6,11].

Photocatalytic activity is strongly dependent on photocatalysts' nanostructure, which is believed to affect the transport and separation efficiencies of photo-generated electrons and holes in the photocatalysts. Thus, the creation of innovative nanomaterials and nanostructures are starting to scale up dramatically. Up to now, various nanostructures, such as one-dimensional nanorods/nanotubes/nanowires, two-dimensional nanosheets/nanoflakes, and three-dimensional nanoporous structures, have been designed for promoted charge transport and enhanced charge separation for high-efficiency photocatalytic hydrogen production [5,6]. Among them, mesoporous materials, especially MCM-41 [12,13], with high specific surface area providing enough surface reactive sites and nanoscale channel wall facilitating transfer of photogenerated charges to surface, are of great potential to act as photocatalysts. However, it is always necessary to activate MCM-41 by introducing transition-metal ions into the mesoporous frameworks, because MCM-41 composed of Si and O atoms is not sensitive to either ultraviolet (UV) or visible light. Indeed, transition-metal incorporated MCM-41 has been well investigated for different photocatalytic applications, including CO₂ reduction, organic pollutant degradation, NO_x decomposition, as well as H₂/O₂ production from water [14–24].

* Corresponding authors. Tel.: +86 29 82668296; fax: +86 29 82669033.

E-mail addresses: shshen.xjtu@mail.xjtu.edu.cn (S. Shen),

Jigang.Zhou@lightsource.ca (J. Zhou).

The generated functionality of optical absorption induced by transition-metal incorporation could be attributed to ligand-to-metal charge-transfer (LMCT) excitation for single-metal incorporated MCM-41, or metal-to-metal charge-transfer (MMCT) excitation for bimetal incorporated MCM-41. Peng et al. [25] determined that Ti-MCM-41 could photocatalytically generate hydrogen from water under UV light irradiation, which was functioned by LMCT excitation with electrons transfer from O^{2-} to Ti^{4+} . We successfully developed Cr/Ti co-incorporated MCM-41 (Cr/Ti-MCM-41), in which the oxo-bridged bimetallic charge-transfer units ($Cr-O-Ti$) acted as a light induced charge-transfer pump based on MMCT excitation. Cr/Ti-MCM-41 was found to have much higher photocatalytic activity for hydrogen production than Cr-MCM-41, due to the suppressed electron-hole recombination in these $Cr-O-Ti$ units [26]. However, there are still only a few reports on transition-metal incorporated MCM-41 for photocatalytic hydrogen production and the hydrogen production activity is very low. Considering the unique superiority of MCM-41 as photocatalyst support, once optically activated by transition-metal incorporation, a systematic investigation on transition-metal incorporated MCM-41 as high efficiency photocatalysts is of great necessity for further improvement in solar hydrogen production.

In the present study, a series of transition metals ($TM = Fe, Co$, and Ni) was successfully incorporated into the mesoporous frameworks of MCM-41, to activate the materials as photocatalysts for solar hydrogen production, based on LMCT excitation for $Fe-$, $Co-$, Ni -MCM-41 and MMCT excitation for $Fe/Co-$, Fe/Ni -MCM-41. The effects of transition-metal (co-)incorporation into MCM-41 on photocatalytic activity for hydrogen production were investigated in detail.

2. Experimental section

2.1. Preparation of transition-metal ($M = Fe, Cr, Ni$) incorporated MCM-41

M-MCM-41 was prepared by a direct hydrothermal synthesis method using cationic surfactant cetyltrimethylammonium bromide (CTAB) as a template and tetraethylorthosilicate (TEOS) as silicon source in basic conditions. Typically, at $40^{\circ}C$, 1.82 g of CTAB was dissolved into a solution containing 45 mL of deionized water and 0.42 g of NaOH, 8.21 mL of TEOS was then added dropwise and stirred vigorously for 1 h for hydrolysis of TEOS. The desired amount of transition metal nitrate aqueous solution was added into the above sol under stirring. The mixture was stirred at $40^{\circ}C$ for another 1 h, and then transferred to a 90-mL Teflon-lined autoclave and held at $100^{\circ}C$ for 3 days. The product obtained was filtered, washed with water and ethanol, and dried in air at $100^{\circ}C$ overnight. To remove the surfactant, the samples were annealed at $520^{\circ}C$ in air for 6 h, with a ramping rate of 10 K/min. For $Fe-$, $Co-$, Ni -MCM-41, the molar ratio of $Fe:Si$, $Co:Si$, or $Ni:Si$ is 0.02:1; for $Fe/Co-$, Fe/Ni -MCM-41, the molar ratio of $Fe:Co:Si$, or $Fe:Ni:Si$ is 0.01:0.01:1.

2.2. Characterization of materials

X-ray diffraction patterns (XRD) were obtained from a PANalytical X'pert MPD Pro diffractometer using Ni-filtered $Cu K\alpha$ irradiation (wavelength 1.5406 Å) the voltage used was 40 kV and the current was 40 mA. N_2 adsorption-desorption isotherms were conducted at 77 K using an Accelerated Surface Area and Porosimetry Analyzer (ASAP 2020, Micromeritics) after degassing the samples at $150^{\circ}C$ for 4 h. Surface area was determined using the Brunauer–Emmett–Teller (BET) methods. Elemental analysis

was conducted on the Bruker S4 PIONEER X-ray fluorescence spectrum (XRF) using Rh target and 4 kW maximum power. Diffuse reflectance UV-vis spectra (UV-vis) were measured on a HITACHI U4100 instrument equipped with lab-sphere diffuse reflectance accessory. Fourier transform infrared spectra (FT-IR) were recorded on a Bruker Vortex 70 FTIR spectrometer using the KBr pellet technique. Transmission electron microscopy (TEM) was carried out in a FEI Tecnai G² F30 microscope working at 300 kV. X-ray photoelectron spectroscopy (XPS) measurements were conducted on a Kratos spectrometer (AXIS Ultra DLD) with monochromatic $Al K\alpha$ radiation ($\hbar\nu = 1486.69$ eV), and with the pressure of sample analysis chamber under high vacuum ($<3 \times 10^{-9}$ Torr). Electron paramagnetic resonance (EPR) experiments were performed on a Bruker EMX X-band spectrometer equipped with a helium cryostat with temperatures $T = 1.82$ K and microwave frequency = 9.4 GHz. The H_2 Temperature-Programmed Reduction (TPR) profiles were carried out on an AutoChem II 2920 (Micromeritics) chemisorption analyzer. Prior to each TPR run, the sample cell was purged with Ar gas (20 cm³/min) at $300^{\circ}C$ for 6 h, and then cooled down to room temperature. After the pretreatment, the samples were tested by increasing the temperature from 40 to $1000^{\circ}C$ at 5 °C/min and keeping the temperature at $1000^{\circ}C$ for 30 min under a continuous flow of 10 vol% H_2 (Ar as balance) at 50 cm³/min. The XANES at the Fe K-edge and Ni K-edge were obtained on the Soft X-ray Microcharacterization Beamline (SXRMB, $\Delta E/E: \sim 10^{-4}$) at the Canadian Light Source (CLS), a 2.9 GeV third generation synchrotron source, using a Si(111) double crystal monochromator and were recorded in bulk sensitive fluorescence yield and/or the surface sensitive total electron yield (TEY).

2.3. Evaluation of photocatalytic activity

Photocatalytic hydrogen evolution was performed using a Pyrex cell. A 300-W Xe lamp was used as the simulated solar light source. Hydrogen gas was analyzed by an online thermal conductivity detector (TCD) gas chromatograph (NaX zeolite column, nitrogen as a carrier gas). In all experiments, an amount of 0.20 g photocatalysts was thoroughly suspended, using a magnetic stirrer with constant rotational velocity, into a CH_3OH aqueous solution (20 vol%, 180 mL) in the Pyrex cell. Nitrogen gas was purged through the cell before reaction in order to remove oxygen. The temperature for all photocatalytic reactions was kept at $35^{\circ}C$. Control experiments showed no appreciable H_2 evolution without irradiation or photocatalysts. All the photocatalysts cannot produce hydrogen in the absence of methanol as sacrificial reagent.

3. Results and discussion

3.1. Textural and structural properties

The transition-metal incorporated MCM-41 is prepared by a hydrothermal method (see Section 2). The molar ratios of transition metal to Si in the obtained transition-metal incorporated MCM-41 are determined to be very close to the initial molar ratios of raw materials (see Supplementary material, Table S1).

Fig. 1A shows the low-angle XRD patterns of transition-metal incorporated MCM-41. MCM-41 has a strong peak at $2\theta = 2^{\circ}-3^{\circ}$ and two weak peaks at $4^{\circ}-5^{\circ}$ corresponding to the (100), (110), and (200) reflections of hexagonal mesoporous structure, respectively. For the transition-metal incorporated MCM-41, the peak intensity of (100) reflection is lower and the (110) and (200) peaks are not observable, due to the less ordered MCM-41 structure induced by transition-metal incorporation. From the wide-angle XRD patterns of transition-metal incorporated MCM-41 (see Supplementary material, Fig. S1), except for the peak assigned to

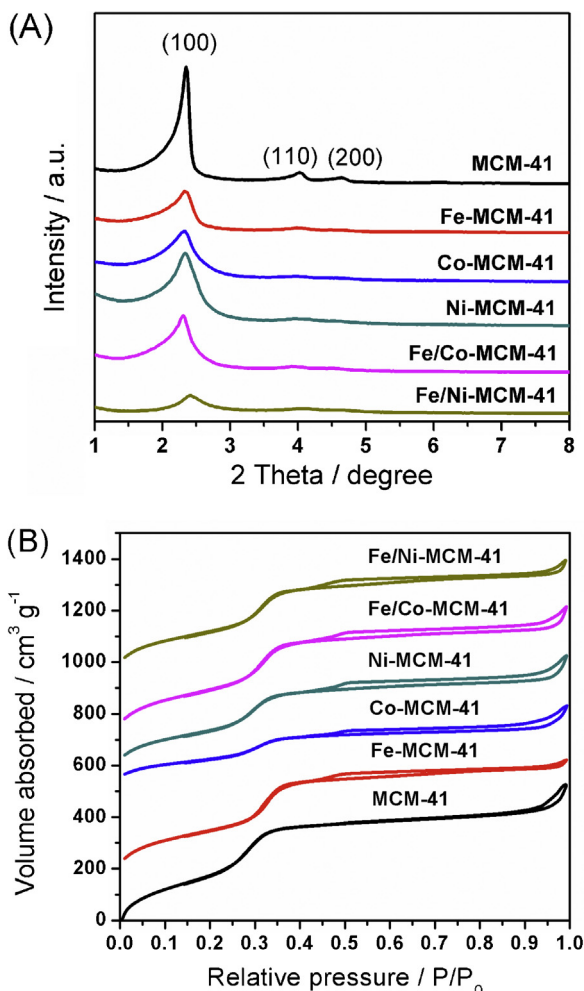


Fig. 1. (A) Low-angle XRD patterns and (B) N₂ adsorption–desorption isotherms of transition-metal incorporated MCM-41.

amorphous silica ($2\theta = 22.5^\circ$), no other peak can be observed. This implies that the transition-metal atoms are highly dispersed into the mesoporous framework structure or the extremely small size of these transition-metal species (<3 nm) is beyond the detection limitation of X-ray, and most likely do not exist as metal oxides outside of the silica framework. N₂ adsorption–desorption isotherms are another powerful technique to determine the mesoporous structure. As depicted in Fig. 1B, an IUPAC type IV adsorption isotherm typical of mesoporous structure is observed for all the samples [27]. The low pressure ($P/P_0 < 0.25$) adsorption is assigned to monolayer–multilayer adsorption of N₂ on the walls of mesopores, while a sharp inflection due to capillary condensation within mesopores appears at relative pressure (P/P_0) between 0.25 and 0.45, which indicates the uniform distribution of the pore size (see Supplementary material, Fig. S2). The inflection moves slightly to higher relative pressure with transition-metal incorporation, indicating an enlargement of pore size.

Based on the low-angle XRD patterns and N₂ adsorption–desorption isotherms, the textural properties of transition-metal incorporated MCM-41 are summarized (see Supplementary material, Table S1). Compared to MCM-41, the d_{100} plane and unit cell size a_0 of most transition-metal incorporated MCM-41 are enlarged. This can be attributed to the isomorphic substitution of framework Si atoms by transition metal atoms due to the higher ionic radii of the transition metal ions (Co²⁺ = 72 pm and Ni²⁺ = 69 pm) in comparison to Si⁴⁺ (40 pm) and due to the

longer bond lengths of Co–O and Ni–O bonds in comparison to Si–O bonds. Thus, the higher ionic radii and the longer M–O bonds (where M = Co²⁺ and Ni²⁺) results in an increase in the unit cell size (a_0) in Ni- and Co-MCM-41 materials in comparison to siliceous MCM-41. However, an opposite tendency of unit cell size is seen for Fe-, and Fe/Ni-MCM-41. Similar observation on metal incorporated MCM-41 was reported by other researchers and this was attributed to the effects of specific synthesis conditions on the wall thickness [28,29], even though the enlarged metal–oxygen (M–O) distance relative to the Si–O distance is expected to enlarge a_0 . The data in Table S1 (see Supplementary material) also demonstrate that the BET surface area is decreased by transition-metal incorporation, whereas the pore volume and pore size are increased. Moreover, the wall thickness of mesopores is decreased for all the transition-metal incorporated MCM-41, when compared to MCM-41. These results suggest the partial collapse of the ordered hexagonal mesopore structure and formation of distortions in the pore wall, which supports that the substitutional incorporation of transition-metal atoms into the Si–O framework so that the crystal integrity of hexagonal mesoporous structure of MCM-41 is partly compromised. As evidenced by TEM images shown in Fig. 2, MCM-41 possesses order mesoporous structure which becomes less order after transition-metal incorporation. Furthermore, one can hardly find nanoparticles or clusters of metal oxides outside the mesoporous structures in TEM images, indicating that most of the transition metal atoms have been incorporated into the Si–O framework of MCM-41 as discussed previously.

Fourier transform infrared spectra (FT-IR) can provide supplementary evidence for framework incorporation of metal ions in MCM-41. In all MCM-41 samples (see Supplementary material, Fig. S3), two obvious FT-IR bands are observed at around 1080 and 808 cm⁻¹, assigned to asymmetric and symmetric Si–O stretching vibrations, respectively [30]. The band at around 960 cm⁻¹ could be assigned to the lattice defect of MCM-41 framework. The variation in the position and strength of this band has been generally used as the evidence of transition-metal incorporated in Si–O framework [26,28,31,32]. A careful check on this band shows that it is slightly shifted to the lower wavenumber (see Supplementary material, Table S2), and its strength becomes more intense relative to that of the symmetric Si–O stretching vibration at 800 cm⁻¹, after transition-metal incorporation. One can also observe similar shift in the asymmetric Si–O stretching vibration at around 1080 cm⁻¹ for these transition-metal incorporated MCM-41 materials (see Supplementary material, Table S2). These observations indicate the successful incorporation of transition metals in the Si–O framework of MCM-41 consistent with observations above in this work.

3.2. Optical properties

The diffuse reflectance UV–vis spectral studies have been considered to be very sensitive in identifying metal ions existing in the framework of mesoporous silica materials. Fig. 3 shows the diffuse reflectance UV–vis spectra of transition-metal incorporated MCM-41. MCM-41 does not exhibit any obvious absorption in the range of 300–800 nm, indicating that it is not sensitive to UV or visible light. In comparison, all the transition-metal incorporated MCM-41 shows optical absorption in UV-visible light region ($\lambda > 400$ nm). In the absorption spectrum of Fe-MCM-41, no obvious absorption band above 500 nm, which is indicative of the formation of iron oxide particles, is observed, while more likely there is an intensive absorption band exists below 300 nm. Similar optical absorption profiles have been reported in other studies on Fe-MCM-41 [33–35]. This suggests that most of the Fe ions have been incorporated into the framework of MCM-41 and are involved in the tetrahedrally coordinated geometry. Co-MCM-41 exhibits three absorption peaks at ca. 525, 595 and 645 nm, suggesting the

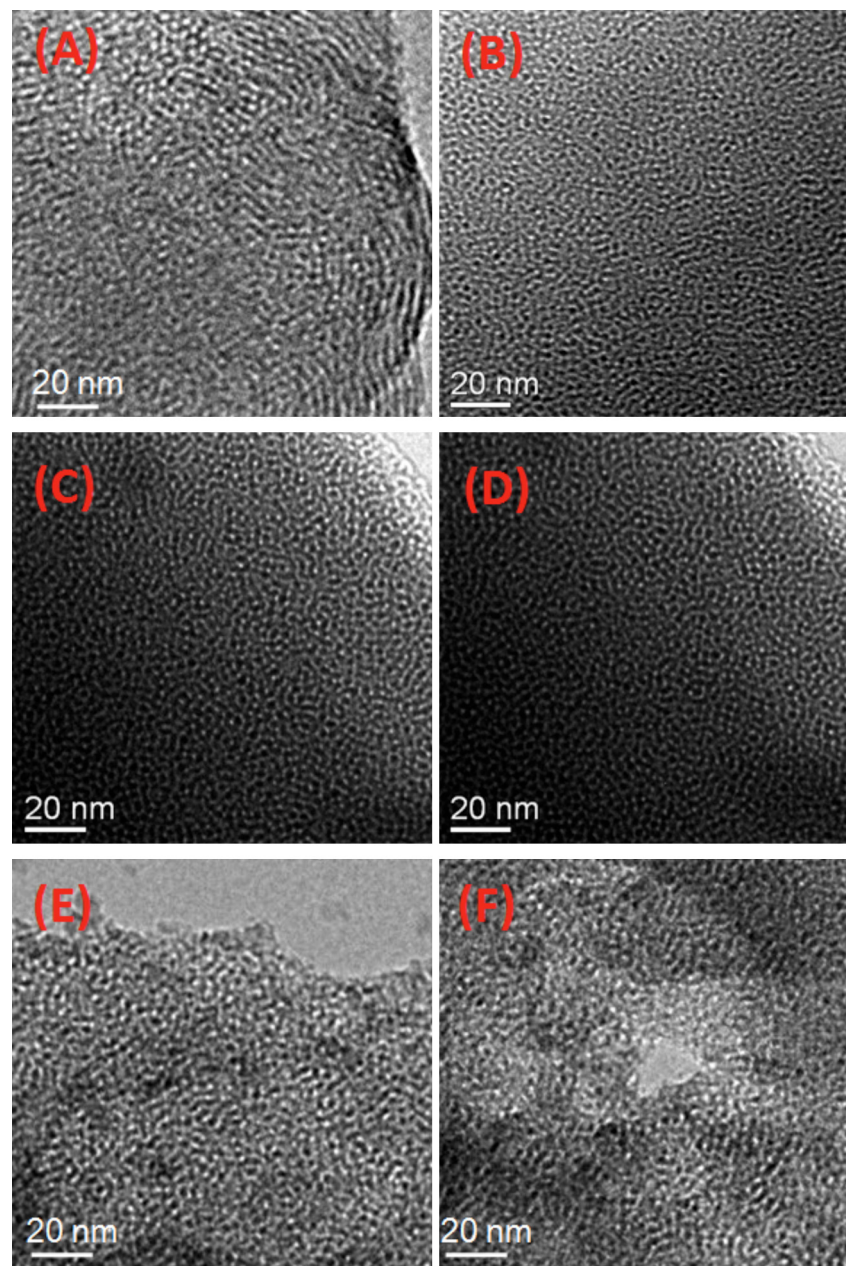


Fig. 2. TEM images of transition-metal incorporated MCM-41. (A) MCM-41, (B) Fe-MCM-41, (C) Co-MCM-41, (D) Ni-MCM-41, (E) Fe/Co-MCM-41, and (F) Fe/Ni-MCM-41.

presence of tetrahedrally coordinated Co^{2+} in the silica framework [36]. Such triplet of absorption bands, which is characteristic of ${}^4\text{A}_2(\text{F}) \rightarrow {}^4\text{T}_1(\text{P})$ ligand field transition of tetrahedrally coordinated Co^{2+} , is caused by Jahn-Teller distortions and/or spin-orbit coupling during the spin-allowed transition [37]. No obvious peaks at *ca.* 300 and 400 nm assigned to Co^{3+} and bulk cobalt oxides (CoO_x) are found [38]. One weak peak is seen at *ca.* 420 nm for Ni-MCM-41, which belongs to tetrahedrally coordinated Ni^{2+} in MCM-41 framework [35].

3.3. Chemical states and coordination environments of incorporated transition metals

XPS spectra are used to determine the chemical states of transition metals incorporated in MCM-41. As shown in Fig. S4 (see Supplementary material), Si 2p and O 1s spectra contains a

single peak centred at 104.0 eV and 533.0 eV, respectively, at values characteristic for the silicates. Fig. 4A shows broad peaks centered at 712.5 eV and 725.4 eV for Fe 2p_{3/2} and Fe 2p_{1/2} spectra. Similar Fe 2p spectra for Fe-MCM-41 has been obtained and carefully investigated by Stefanis et al. [34], which could be de-convoluted to eight peaks divided in four pairs of 2p spin-orbit split doublets, indicating the existence of both Fe^{2+} and Fe^{3+} in Fe-, Fe/Co-, and Fe/Ni-MCM-41. The main cause of the existence of different oxidation states of iron is due to the migration of tetrahedrally coordinated Fe^{3+} toward the surface of the pore wall and the reduction of Fe^{3+} to Fe^{2+} by $-\text{OH}$ groups, during the high temperature treatment to remove the surfactant [39]. The Co 2p_{3/2} peak shown in Co 2p spectra (Fig. 4B) is located at *ca.* 782.3 eV and can be assigned to Co^{2+} [40], and indicative of successful incorporation of Co^{2+} into the framework of MCM-41 for Co-MCM-41 and Fe/Co-MCM-41, because no Co 2p_{3/2} peak assigned to metal oxide species

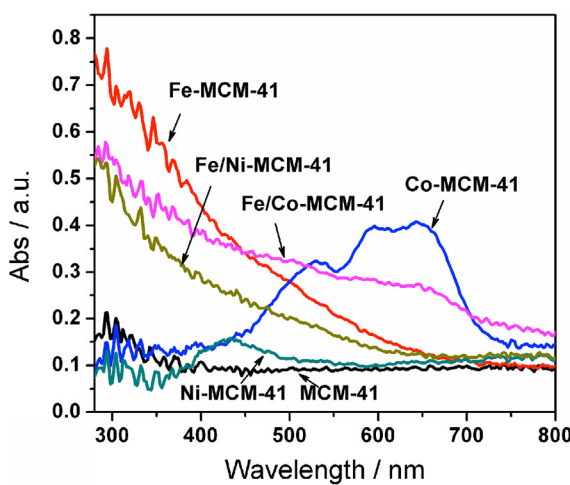


Fig. 3. Diffuse reflectance UV–vis spectra of transition-metal incorporated MCM-41.

of Co_3O_4 (*ca.* 779.8 eV), Co_2O_3 (*ca.* 779.6 eV) and CoO (*ca.* 780.4 eV) can be observed [41]. Similarly, the Ni^{2+} $2\text{p}_{3/2}$ XPS peaks are located at 857.0 eV in Fig. 4C and have obviously shifted to higher binding energy, when compared to the Ni^{2+} $2\text{p}_{3/2}$ peak positions for nickel oxide species [41,42]. This may be because of the stronger Ni–O chemical bonds for tetrahedrally coordinated Ni^{2+} in MCM-41 framework.

The coordination environment of transition metals in the incorporated MCM-41 was further analyzed by electron paramagnetic resonance (EPR) measurements. The EPR spectrum of Fe-MCM-41 is shown in Fig. 5A. The signal at $g=5.5$ is assigned to Fe^{3+} in less distorted tetrahedral sites. The signal corresponding to $g=4.3$ is usually considered as evidence of the presence of framework Fe^{3+} ions and is typical of isolated Fe^{3+} paramagnetic ions in a strong rhombic distorted tetrahedral coordination. The signal at $g=2.0$ could also be partly due to Fe^{3+} in tetrahedral site as observed by Goldfarb et al. [43], although this signal has been also assigned to extra-framework Fe^{3+} or Fe^{3+} species in octahedral coordination [44,45]. Obvious signals at $g=2.3$ – 2.5 , ascribed to iron clusters or iron oxide species [46], cannot be observed. Thus, it could be deduced that Fe^{3+} ions mainly exist in tetrahedral coordination in the framework of MCM-41 [47,48], which is consistent with UV–vis spectra analysis results. In Fig. 5B, the large signal at $g=5.36$ is shown for the EPR spectra of Co-MCM-41, which corresponds to high-spin Co^{2+} species, while the small signal ($g=2.0$) may be assigned to a low-spin $\text{Co}-\text{O}_2$ adduct or an organic radical generated during thermal decomposition of the template [49]. In other study, the signal near $g=2.0$ was also assigned to the Co^{2+} species [50]. We do not find any obvious signal in the EPR spectra of Ni-MCM-41 (figure not shown), as Ni^{2+} is EPR silent when measured at 9 GHz [51]. Fe/Co- and Fe/Ni-MCM-41 show the EPR spectra similar to Fe-MCM-41 (see Supplementary material, Fig. S5), because EPR signals of Fe-MCM-41 are much stronger than those of Co- and Ni-MCM-41.

Temperature programmed reduction (TPR) has been employed to investigate the reduction characteristics of transition metals incorporated into MCM-41, and the TPR profiles are shown in Fig. S6 (see Supplementary material). Fe-MCM-41 displays broad peaks in the temperature range of 650–850 K, which suggests the reduction of the incorporated Fe^{3+} to Fe^{2+} , as supported by the similar TPR results reported previously [48,52]. Co-MCM-41 shows reduction peak beginning at *ca.* 900 K which is much higher than reduction temperature of supported Co ions [53]. Thus, it can be deduced that Co has been incorporated into MCM-41 framework in Co-MCM-41 in the present study since the strong interaction between Co

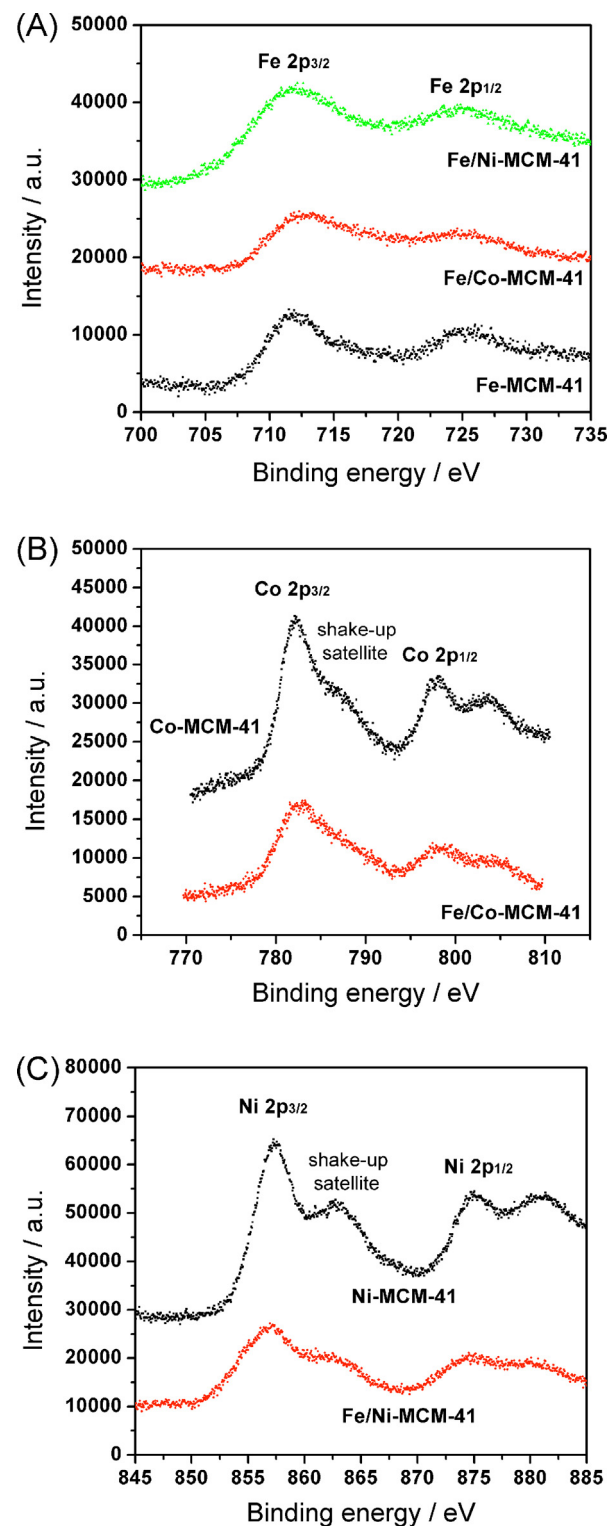


Fig. 4. XPS spectra of transition-metal incorporated MCM-41. (A) Fe 2p spectra, (B) Co 2p spectra, (C) Ni 2p spectra.

and Si via the formation of $\text{Co}-\text{O}-\text{Si}$ bonds. Ni-MCM-41 does not show any reduction below 800 K, which suggests that the presence of extra-framework nickel oxides can be ruled out, and thus successful incorporation of Ni into the framework of MCM-41 as in Co-MCM-41 is indicated. After co-incorporation of Ni^{2+} or Co^{2+} with Fe^{3+} into MCM-41, the reduction peaks of Fe^{3+} to Fe^{2+} for Fe/Co- and Fe/Ni-MCM-41 are observed at higher temperatures,

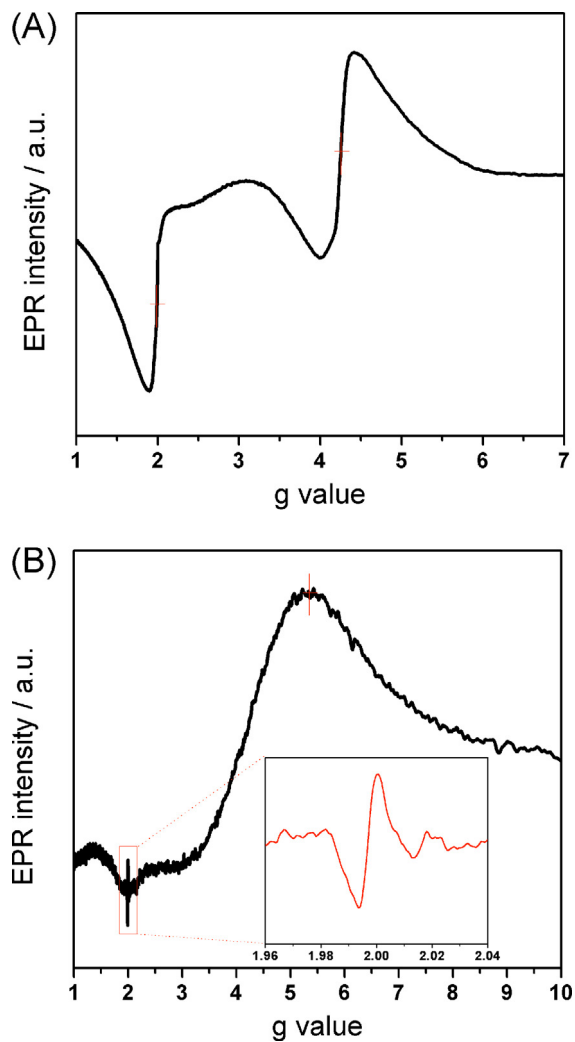


Fig. 5. EPR spectra of (A) Fe-MCM-41 and (B) Co-MCM-41. The inset shows an enlarged portion of the ESR spectrum.

when compared to Fe-MCM-41. This might be due to the formation of oxo-bridged Fe–O–M ($M = \text{Co, Ni}$) structure, which further stabilizes Fe^{3+} incorporated in MCM-41.

To further confirm the oxo-bridge structures in bimetal incorporated MCM-41, local environment of Fe and Ni was studied by means of Fe and Ni K-edge high-resolution X-ray absorption near edge structure (XANES) spectroscopy to compare the oxidation state and coordination number of metal ions in both single-metal and bimetal incorporated MCM-41 samples [54]. Fig. 6A shows the Fe K-edge XANES spectra of Fe-MCM-41 and Fe/Ni-MCM-41 at fluorescence yield mode. The pre-edge peak displays small but reproducible variation in the peak intensity between Fe-MCM-41 and Fe/Ni-MCM-41, which is indicative of significant changes in the Fe coordination number. The increased pre-edge peak density reveals that Fe in Fe/Ni-MCM-41 has a better tetrahedral coordination compared to that in Fe-MCM-41 [55]. This point has been further supported by the Fourier transforms of k^3 -weighted Fe K-edge EXAFS spectra (Fig. 6B) for Fe-MCM-41 and Fe/Ni-MCM-41 where an enhanced Fe–O peak at $\sim 1.5\text{\AA}$ is shown in Fe/Ni-MCM-41 relative to that in Fe-MCM-41 [56]. This change must be caused by Ni incorporation which stabilizes Fe–O in Si–O matrix which has a tetrahedral geometry. Ni K-edge XANES spectra at fluorescence mode of Ni-MCM-41 and Fe/Ni-MCM-41 are shown in Fig. 6C. Note that the pre-edge peak shifts slightly to higher energy for Fe/Ni-MCM-41 when compared to Ni-MCM-41. This means that

Ni oxidation increases a little which might be due to the partial replacement of Ni^{2+} –O– Ni^{2+} by Fe^{3+} –O– Ni^{2+} in Fe/Ni-MCM-41. Fe K-edge XANES spectra of Fe-MCM-41 and Fe/Ni-MCM-41 were also recorded in the surface sensitive total electron yield (TEY) with use of specimen current (Fig. 6D). The pre-edge peak position depends mainly on the mean Fe oxidation state, gradually increasing from Fe^{2+} to Fe^{3+} . As indicated by XPS results, Fe is mainly in Fe^{3+} in both Fe-MCM-41 and Fe/Ni-MCM-41 which has been confirmed again by Fe K-edge XANES recorded in bulk sensitive fluorescence yield mode (Fig. 6A). XPS also shows the possibility of surface reduction (more Fe^{2+} on surface) in Fe-MCM-41 by the formation of Fe^{2+} –OH groups. Thus, the slight shift of pre-edge peak to higher energy in Fe/Ni-MCM-41 in Fig. 6D should be related to the substitution of Fe^{2+} –OH surface groups to form oxo-bridged Fe^{3+} –O– Ni^{2+} structure by the co-incorporation of Ni into MCM-41 framework [55]. All of those spectroscopy observations strongly support the formation of oxo-bridged Fe–O–Ni structure in Fe/Ni-MCM-41. Along with the K-edge XAFS, we also collected surface sensitive Fe and Ni L-edge XANES at TEY mode (shown Fig. 6E and F) which again support the formation of Fe^{3+} –O– Ni^{2+} oxo structure stabilizing the Fe^{3+} and Ni^{2+} in Fe/Ni-MCM-41 relative to that in Fe-MCM-41 and Ni-MCM-41, respectively. The structure change at Fe and also Ni side upon co-existence with the other element is apparent as seen in the L-edge XANES, where the absorption shape and edge position are sensitive to the local environment and oxidation state: co-existence of Ni makes a more “oxidized” Fe in Fe/Ni-MCM-41 (a higher peak ratio of 711 eV peak over the peak at 709 eV, Fig. 6E) relative to that in Fe-MCM-41; while co-existence of Fe results in a less “oxidized” Ni in Fe/Ni-MCM-41 (negatively shifted absorption edge, Fig. 6F) relative to that in Ni-MCM-41.

3.4. Photocatalytic activity and proposed mechanism

The photocatalytic activities of these transition-metal incorporated MCM-41 were evaluated for hydrogen production from aqueous solution containing methanol as sacrificial reagent under irradiation from Xe lamp. As shown in Fig. 7, MCM-41 does not exhibit any photocatalytic activity for hydrogen production, due to its non-response to light. After incorporating Fe, Co, Ni into MCM-41, the photocatalytic activities are enhanced in order of $\text{Fe} > \text{Co} \approx \text{Ni}$ -MCM-41. Especially, Fe-MCM-41 shows the highest photocatalytic activity, with the very stable hydrogen production rate reaching $112.5\text{ }\mu\text{mol/h/g}_{\text{cat}}$ (see Supplementary material, Fig. S7) in the 72-h photocatalytic reaction period (see Supplementary material, Fig. S8). For Co- and Ni-MCM-41, the photocatalytic activities could be further enhanced by co-incorporation of Fe into the silica framework. When compared to Fe- and Ni-MCM-41, the photocatalytic activity of Fe/Ni-MCM-41 are increased by ~ 1.3 and ~ 16.7 times, respectively, to be $141.9\text{ }\mu\text{mol/h/g}_{\text{cat}}$ (see Supplementary material, Fig. S7). No leaching and unchanged oxidation states of Fe and Ni ions after photocatalytic reaction, as confirmed by XRF and XPS analysis (data not shown), respectively, again indicates the stability and recyclability of these metal incorporated MCM-41 for photocatalytic hydrogen generation. Similar enhancement in photocatalytic hydrogen evolution activity was also observed for Cr/Ti-MCM-41 which displayed much higher photocatalytic activity than Cr-MCM-41, mainly due to the promoted charge separation via the oxo-bridged Cr–O–Ti structure [26]. Although direct comparison on the photocatalytic activities of Cr/Ti-MCM-41 and Fe/Ni-MCM-41 is not reasonable, because of the different photocatalytic systems (aqueous solutions, light sources, etc.), it could be still deduced that the oxo-bridged structure created by bimetal incorporation gives rise to promoted charge separation and hence enhanced photocatalytic activity for hydrogen evolution.

On the basis of the characterization results described earlier, it is indicative that transition metals have been tetrahedrally

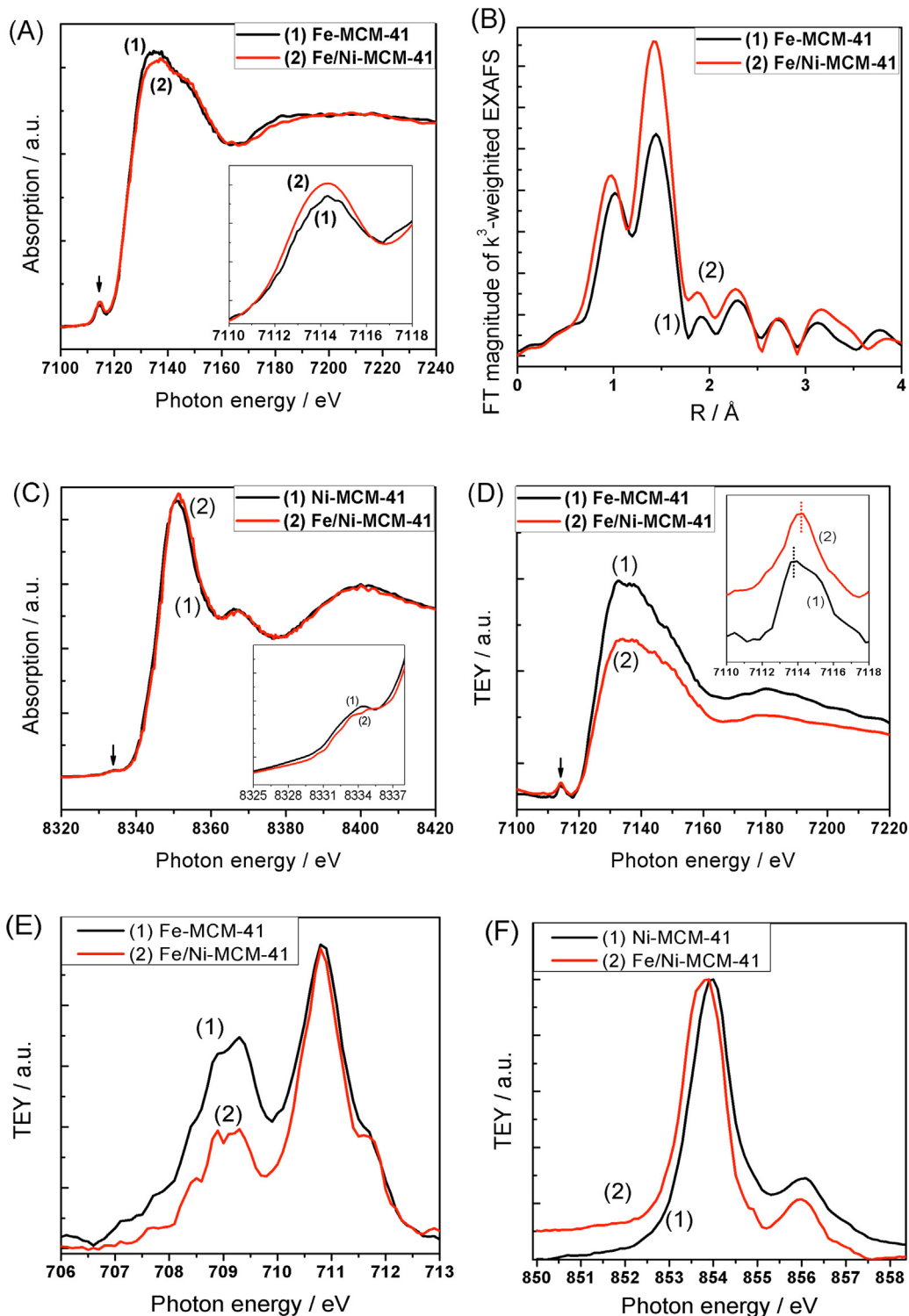
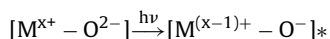


Fig. 6. (A) Fe K-edge XANES spectra of Fe-MCM-41 and Fe/Ni-MCM-41, (B) Fourier transforms of k^3 -weighted Fe K-edge EXAFS spectra of Fe-MCM-41 and Fe/Ni-MCM-41, (C) Ni K-edge XANES spectra of Ni-MCM-41 and Fe/Ni-MCM-41, (D) Fe K-edge XANES spectra of Fe-MCM-41 and Fe/Ni-MCM-41 recorded in TEY, (E) Fe L-edge XANES spectra of Fe-MCM-41 and Fe/Ni-MCM-41 recorded in TEY, (F) Ni L-edge XANES spectra of Ni-MCM-41 and Fe/Ni-MCM-41 recorded in TEY.

coordinated (or distorted tetrahedral in case of Fe-MCM-41) and incorporated into the framework of MCM-41, and act as the light sensitizers for photocatalytic hydrogen production. It is generally accepted that the photocatalytic mechanism of transition-metal incorporated MCM-41 is based on ligand to metal charge-transfer (LMCT) excitation. Tetrahedrally coordinated M–O (M = Fe, Co, and Ni) chromophores dispersed in MCM-41 can be easily excited under

UV and/or visible-light irradiation to form corresponding charge-transfer excited states:



The electrons and holes produced by excitation always have stronger reduction and oxidation abilities than the charges generated in the corresponding bulk semiconductor photocatalyst. In the

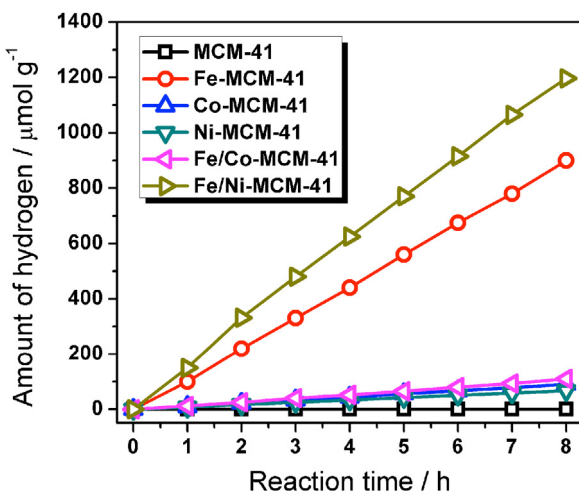


Fig. 7. Time dependent photocatalytic hydrogen production over transition-metal incorporated MCM-41 under the irradiation from 300 W Xe lamp as simulated solar light.

case of Fe-MCM-41, the $[Fe^{2+}-O^-]^*$ excited states can donate electrons to reduce water for hydrogen generation. After the electron and hole reacts with water and sacrificial reagent, respectively, the $[Fe^{2+}-O^-]^*$ excited states return back to be $[Fe^{3+}-O^{2-}]$. This catalytic cycle keeps Fe ions in 3+ oxidation state, and contributes to the good photocatalytic stability for hydrogen production in Fe-MCM-41 (see Supplementary material, Fig. S8). In comparison, Co-, and Ni-MCM-41 show very low photocatalytic activity for hydrogen production (Fig. 7), although they can absorb visible light ($\lambda > 400$ nm) (Fig. 3). It was previously reported that the incorporation of certain transition metals was deleterious for photodegradation under UV light, as the transition-metal ions could accelerate the electron and hole recombination by acting as intermediate levels [35]. Especially for Co-MCM-41, as analyzed based on UV-vis spectra, the triple-split $^4A_2(F) \rightarrow ^4T_1(P)$ transition creates discrete suborbitals acting as recombination sites for photoinduced charges. This could be the main reason for the low photocatalytic activity of Co-MCM-41. For Ni-MCM-41, the weak optical absorption in UV-visible light region may be another possible reason for its poor photocatalytic activity.

After co-incorporating Fe into Co- and Ni-MCM-41, the photocatalytic activity for hydrogen production could be enhanced (Fig. 7 and see Supplementary material, Fig. S7). The resulting Fe/Co- and Fe/Ni-MCM-41 show photocatalytic activity 1.2 and 16.7 times higher than Co- and Ni-MCM-41, respectively. Considering the photocatalytic activity of Fe-MCM-41 \gg Co-MCM-41, it's reasonable that Fe/Co-MCM-41 exhibits photocatalytic activity higher than Co-MCM-41 but lower than Fe-MCM-41. However, unlike Fe/Co-MCM-41, Fe/Ni-MCM-41 exhibits superior photocatalytic activity compared to both of the single metal incorporated counterparts (i.e., Fe- and Co-MCM-41), as well as the simple sum of Fe-MCM-41 + Ni-MCM-41 (see Supplementary material, Fig. S7). Thus, the synergistic effect of Fe^{2+} and Fe^{3+} co-incorporated in MCM-41 could then be responsible for the high photocatalytic activity, which could be attributed to its high efficiency in charge formation and separation. It has been reported that bi-metal modified (or incorporated) MCM-41 exhibited excellent photocatalytic activity for hydrogen generation and CO_2 reduction [15,16,26,56–58], which was believed to be based on the metal-to-metal charge-transfer (MMCT) excitation as indicated below:

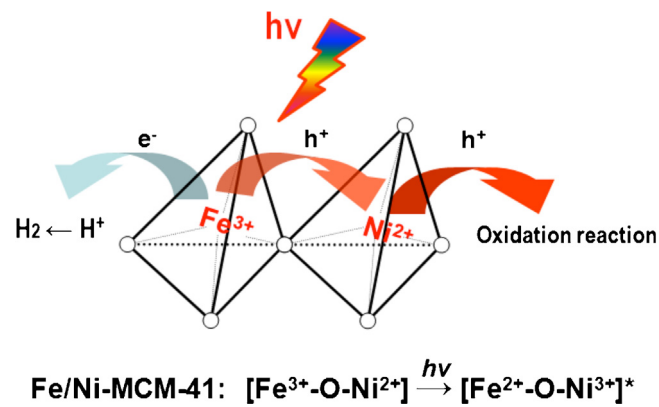
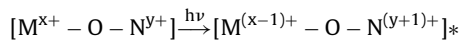


Fig. 8. Schematic of charge carrier transfer process in Fe/Ni-MCM-41.

The $M^{(x-1)+}$ and $N^{(y+1)+}$ species of $[M^{(x-1)+}-O-N^{(y+1)+}]^*$ excited states can donate electrons and holes involved in photocatalytic reduction and oxidation half reactions, respectively. In the case of Fe/Ni-MCM-41, the excitation of $[Fe^{3+}-O-Ni^{2+}] \rightarrow [Fe^{2+}-O-Ni^{3+}]^*$ is accompanied with complete transfer of an electron from donor to acceptor center via oxo-bridge, as shown in Fig. 8, which results in efficient charge separation and creation of long lived electrons and holes to initiate redox reaction [57]. *In situ* XANES at Ni K-edge of photoexcited Fe/Ni-MCM-41 shall find spectroscopic evidence of Ni^{3+} species which will be carried out in the future. As to the $[Fe^{2+}-O-Ni^{3+}]^*$ moieties in photoexcited Fe/Ni-MCM-41, Fe^{2+} and Ni^{3+} acts as electron donor and acceptor with redox potentials appropriate for driving water reduction and sacrificial reagent (methanol) oxidation, respectively. In Fe/Co-MCM-41, the $[Fe^{2+}-O-Co^{3+}]^*$ moieties initiate oxidation reaction with Co^{3+} as electron acceptor. Its lower photocatalytic activity for hydrogen production is consistent with the substantially lower oxidation power of Co^{3+} compared to Ni^{3+} (the redox potential of Co^{3+}/Co^{2+} is ca. 0.3 V lower than that of Ni^{3+}/Ni^{2+}) [59], which limits the reactivity of photocatalytic oxidation process. Thus, the high photocatalytic activity of Fe/Ni-MCM-41 seems explainable, although further investigation is necessary for the clarification of the intrinsic mechanism. Nevertheless, activating mesoporous silica with high surface area in UV and/or visible light region, by creating oxo-bridged MMCT chromophores (bimetallic redox sites) with donor and acceptor redox potential suitable in principle for driving hydrogen generation (or CO_2 reduction) reactions, offers new opportunities for exploring demanding photochemical transformations for solar energy conversion.

4. Conclusion

In summary, MCM-41 mesoporous silica was successfully activated for photocatalytic hydrogen production by incorporating transition metals (Fe, Co, Ni) into its framework. The transition-metal ions were supposed to be well dispersed in the Si-O framework mainly with tetrahedral coordination. Among those single metal incorporated MCM-41, Fe-MCM-41 exhibited the highest photocatalytic activity for hydrogen production, based on the ligand to metal charge-transfer (LMCT) excitation. The photocatalytic activity of Fe-MCM-41 could be further enhanced by incorporating the second transition metal Ni into Si-O framework. The synergistic effect of Ni and Fe co-incorporation is responsible for the high photocatalytic activity for hydrogen production, which could be attributed to its high efficiency in charge formation and separation, based on metal-to-metal charge-transfer (MMCT) excitation.

Acknowledgments

The authors gratefully acknowledge the financial support of the National Natural Science Foundation of China (no. 51102194, no. 51121092), the Doctoral Program of the Ministry of Education (no. 20110201120040) and the National Basic Research Program of China (no. 2009CB220000). One of the authors (S. Shen) was supported by the Foundation for the Author of National Excellent Doctoral Dissertation of P. R. China (No. 201335) and the “Fundamental Research Funds for the Central Universities”. The authors also would like to thank Canadian Light Source Inc. for the XAS measurement support.

Appendix A. Supplementary data

Supplementary data associated with this article can be found, in the online version, at <http://dx.doi.org/10.1016/j.apcatb.2013.12.014>.

References

- [1] A. Fujishima, K. Honda, *Nature* 238 (1972) 37.
- [2] A. Kudo, Y. Miseki, *Chem. Soc. Rev.* 38 (2009) 253.
- [3] F.E. Osterloh, *Chem. Mater.* 20 (2008) 35.
- [4] H. Tong, S. Ouyang, Y. Bi, N. Umezawa, M. Oshikiri, J. Ye, *Adv. Mater.* 24 (2012) 229.
- [5] X. Chen, S. Shen, L. Guo, S.S. Mao, *Chem. Rev.* 110 (2010) 6503.
- [6] S. Shen, J. Shi, P. Guo, L. Guo, *Int. J. Nanotechnol.* 8 (2011) 523.
- [7] S. Shen, S.S. Mao, *Nanophotonics* 1 (2012) 31.
- [8] K. Maeda, K. Teramura, K. Domen, *J. Catal.* 254 (2008) 198.
- [9] X. Chen, L. Liu, P.Y. Yu, S.S. Mao, *Science* 331 (2011) 746.
- [10] M. Liu, L. Wang, G. Lu, X. Yao, L. Guo, *Energy Environ. Sci.* 4 (2011) 1372.
- [11] K. Maeda, K. Domen, *J. Phys. Chem. C* 111 (2007) 7851.
- [12] C.T. Kresge, M.E. Leonowicz, W.J. Roth, J.C. Vartuli, J.S. Beck, *Nature* 359 (1992) 710.
- [13] J.S. Beck, J.C. Vartuli, W.J. Roth, M.E. Leonowicz, C.T. Kresge, K.D. Schmitt, C.T.W. Chu, D.H. Olson, E.W. Sheppard, S.B. McCullen, J.B. Higgins, J.L. Schlenkert, *J. Am. Chem. Soc.* 114 (1992) 10834.
- [14] R. Nakamura, A. Okamoto, H. Osawa, H. Irie, K. Hashimoto, *J. Am. Chem. Soc.* 129 (2007) 9596.
- [15] W. Lin, H. Frei, *J. Am. Chem. Soc.* 127 (2005) 1610.
- [16] R. Nakamura, H. Frei, *J. Am. Chem. Soc.* 128 (2006) 10668.
- [17] V.R. Elías, E.V. Sabre, E.L. Winkler, M.L. Satuf, E. Rodriguez-Castellón, S.G. Casuscelli, G.A. Eimer, *Microporous Mesoporous Mater.* 163 (2012) 85.
- [18] H. Shankar, G. Rajasudha, A. Karthikeyan, V. Narayanan, A. Stephen, *Nanotechnology* 19 (2008) 315711.
- [19] S.H. Liu, H.P. Wang, *Int. J. Hydrogen Energy* 27 (2002) 859.
- [20] S.-H. Liu, Y.-J. Huang, K.-S. Lin, M.-C. Hsiao, *Energy Sources* 25 (2003) 591.
- [21] S. Higashimoto, Y. Hu, R. Tsumura, K. Iino, M. Matsuoka, H. Yamashita, Y.G. Shul, M. Che, M. Anpo, *J. Catal.* 235 (2005) 272.
- [22] Y. Hu, G. Martra, J. Zhang, S. Higashimoto, S. Coluccia, M. Anpo, *J. Phys. Chem. B* 110 (2006) 1680.
- [23] S. Rodrigues, K.T. Ranjit, S. Uma, I.N. Martyanov, K.J. Klabunde, *J. Catal.* 230 (2005) 158.
- [24] Y. Hu, Y. Nagai, D. Rahmawaty, C. Wei, M. Anpo, *Catal. Lett.* 124 (2008) 80.
- [25] R. Peng, D. Zhao, N.M. Dimitrijevic, T. Rajh, R.T. Koodali, *J. Phys. Chem. C* 116 (2012) 1605.
- [26] S. Shen, L. Guo, *Catal. Today* 129 (2007) 414.
- [27] K.S.W. Sing, D.H. Everett, R.A.W. Haul, L. Moscou, *Pure Appl. Chem.* 57 (1985) 603.
- [28] Z. Zhu, Z. Chang, L. Kevan, *J. Phys. Chem. B* 103 (1999) 2680.
- [29] R. Portela, M.C. Caneira, B. Sánchez, F.C. Marques, A.M. Stumbo, R.F. Tessinari, J.M. Coronado, S. Suárez, *Appl. Catal., B* 84 (2008) 643.
- [30] Y. Kong, H. Zhu, G. Yang, X. Guo, W. Hou, Q. Yan, M. Gu, C. Hu, *Adv. Funct. Mater.* 14 (2004) 816.
- [31] J.-J. Zou, Y. Liu, L. Pan, L. Wang, X. Zhang, *Appl. Catal., B* 95 (2010) 439.
- [32] S.V. Awate, N.E. Jacob, S.S. Deshpande, T.R. Gaydhankar, A.A. Belhekar, *J. Mol. Catal. A: Chem.* 226 (2005) 149.
- [33] J.-S. Choi, S.-S. Yoon, S.-H. Jang, W.-S. Ahn, *Catal. Today* 111 (2006) 280.
- [34] D. Stefanis, S. Kaciulis, L. Pandolfi, *Microporous Mesoporous Mater.* 99 (2007) 140.
- [35] E.P. Reddy, B. Sun, P.G. Smirniotis, *J. Phys. Chem. B* 108 (2004) 17198.
- [36] S. Lim, D. Ciuparu, C. Pak, F. Dobek, Y. Chen, D. Harding, L. Pfefferle, G. Haller, *J. Phys. Chem. B* 107 (2003) 11048.
- [37] Q. Tang, Q. Zhang, H. Wu, Y. Wang, *J. Catal.* 230 (2005) 384.
- [38] A. Verberckmoes, M.G. Uytterhoeven, R.A. Schoonheydt, *Zeolites* 19 (1997) 180.
- [39] E.P. Reddy, L. Davydov, P.G. Smirniotis, *J. Phys. Chem. B* 106 (2002) 3394.
- [40] X. Liu, J. He, L. Yang, Y. Wang, S. Zhang, W. Wang, J. Wang, *Catal. Commun.* 11 (2010) 710.
- [41] M.C. Biesingera, B.P. Payne, A.P. Grosvenor, L.W.M. Lau, A.R. Gerson, R. St. C. Smart, *Appl. Surf. Sci.* 257 (2011) 2717.
- [42] D. Eliche-Quesada, J. Mérida-Robles, P. Maireles-Torres, E. Rodríguez-Castellón, A. Jiménez-López, *Langmuir* 19 (2003) 4985.
- [43] D. Goldfarb, M. Bernardo, K.G. Strohmaier, D.E.W. Vaughan, H. Thomann, *J. Am. Chem. Soc.* 116 (1994) 6344.
- [44] N. Gokulakrishnan, A. Pandurangan, P.K. Sinha, *J. Chem. Technol. Biotechnol.* 82 (2007) 25.
- [45] S.V. Sirotin, I.F. Moskovskaya, B.V. Romanovsky, *Catal. Sci. Technol.* 1 (2011) 971.
- [46] A. Tuel, I. Arcon, J.M.M. Millet, *J. Chem. Soc. Faraday Trans.* 94 (1998) 3501.
- [47] B. Li, K. Wu, T. Yuan, C. Han, J. Xu, X. Pang, *Microporous Mesoporous Mater.* 151 (2012) 277.
- [48] P.B. Amama, S. Lim, D. Ciuparu, Y. Yang, L. Pfefferle, G.L. Haller, *J. Phys. Chem. B* 109 (2005) 2645.
- [49] J.F. Díaz, K.J. Balkus Jr., *Chem. Mater.* 9 (1997) 61.
- [50] A.M. Morey, N. Li, W.A. Hines, D.M. Perry, M. Jain, G.L. Haller, S.L. Sui, *J. Appl. Phys.* 110 (2011) 103904.
- [51] T.A. Konovalova, Y. Gao, R. Schad, L.D. Kispert, C.A. Saylor, L.-C. Brunel, *J. Phys. Chem. B* 105 (2001) 7459.
- [52] Á. Szegedi, G. Pál-Borbély, K. Lázár, *React. Kinet. Catal. Lett.* 74 (2001) 277.
- [53] T. Jiang, Q. Zhao, H. Yin, M. Li, *J. Porous Mater.* 14 (2007) 457.
- [54] W. Lin, H. Frei, *J. Phys. Chem. B* 109 (2005) 4929.
- [55] G. Giuli, E. Paris, G. Pratesi, C. Koebel, C. Cipriani, *Meteorit. Planet. Sci.* 38 (2003) 1181.
- [56] Y. Wang, Q. Zhang, T. Shishido, K. Takehira, *J. Catal.* 209 (2002) 186.
- [57] X. Wu, W.W. Weare, H. Frei, *Dalton Trans.* 45 (2009) 10114.
- [58] W. Lin, H. Frei, *C.R. Chim.* 9 (2006) 207.
- [59] J. Yang, J.J. Xu, *J. Electrochem. Soc.* 153 (2006) A716.